

Angle-resolved photoemission spectroscopy of perovskite-type transition-metal oxides and their analyses using tight-binding band structure

H. Wadati,^{1,*} T. Yoshida,¹ A. Chikamatsu,² H. Kumigashira,²
M. Oshima,² H. Eisaki,³ Z.-X. Shen,⁴ T. Mizokawa,¹ and A. Fujimori¹

¹*Department of Physics and Department of Complexity Science and Engineering,
University of Tokyo, Kashiwa, Chiba 277-8561, Japan*

²*Department of Applied Chemistry, University of Tokyo,
Bunkyo-ku, Tokyo 113-8656, Japan*

³*National Institute of Advanced Industrial Science and Technology, Tsukuba 305-8568, Japan*

⁴*Department of Applied Physics and Stanford Synchrotron Radiation Laboratory,
Stanford University, Stanford, California 94305, USA*

(Dated: October 30, 2018)

Abstract

Nowadays it has become feasible to perform angle-resolved photoemission spectroscopy (ARPES) measurements of transition-metal oxides with three-dimensional perovskite structures owing to the availability of high-quality single crystals of bulk and epitaxial thin films. In this article, we review recent experimental results and interpretation of ARPES data using empirical tight-binding band-structure calculations. Results are presented for SrVO₃ (SVO) bulk single crystals, and La_{1-x}Sr_xFeO₃ (LSFO) and La_{1-x}Sr_xMnO₃ (LSMO) thin films. In the case of SVO, from comparison of the experimental results with calculated surface electronic structure, we concluded that the obtained band dispersions reflect the bulk electronic structure. The experimental band structures of LSFO and LSMO were analyzed assuming the G-type antiferromagnetic state and the ferromagnetic state, respectively. We also demonstrated that the intrinsic uncertainty of the electron momentum perpendicular to the crystal surface is important for the interpretation of the ARPES results of three-dimensional materials.

INTRODUCTION

Perovskite-type $3d$ transition-metal (TM) oxides have been attracting much interest in these decades because of their intriguing physical properties, such as metal-insulator transition (MIT), colossal magnetoresistance (CMR), and ordering of spin, charge, and orbitals [1]. Early photoemission studies combined with cluster-model analyses have revealed that their global electronic structure is characterized by the TM $3d$ - $3d$ on-site Coulomb interaction energy denoted by U , the charge-transfer energy from the occupied O $2p$ orbitals to the empty TM $3d$ orbitals denoted by Δ , and the p - d hybridization strength denoted by $(pd\sigma)$ [2]. If $\Delta > U$, the band gap is of the d - d type, and the compound is called a Mott-Hubbard-type insulator. For $\Delta < U$, the band gap is of the p - d type: the O $2p$ band is located between the upper and lower Hubbard bands, and the compound is called a charge-transfer-type insulator. In going from lighter to heavier $3d$ TM elements, the d level is lowered and therefore Δ is decreased, whereas U is increased. Thus Ti and V oxides become Mott-Hubbard-type compounds and Mn, Fe, Co, Ni, and Cu oxides charge-transfer-type compounds.

Having established the global electronic structure picture of the transition-metal oxides with their chemical trend, the next step is to understand the momentum dependence of the electronic states, that is, the “band structure” of the hybridized p - d states influenced by the Coulomb interaction U . Angle-resolved photoemission spectroscopy (ARPES) is a unique and most powerful experimental technique by which one can directly determine the band structure of a material. However, ARPES studies have been largely limited to low-dimensional materials and there have been few studies on three-dimensional TM oxides with cubic perovskite structures because many of them do not have a cleavage plane. Recently, Yoshida *et al.* succeeded in cleaving single crystals of SrVO_3 (SVO) along the cubic (100) surface and performed ARPES measurements [3]. Another way of performing ARPES studies of such materials is the use of single-crystal thin films. Recently, high-quality perovskite-type oxide single-crystal thin films grown by the pulsed laser deposition (PLD) method have become available [4, 5], and setups have been developed for their *in-situ* photoemission measurement [6, 7]. By using well-defined surfaces of epitaxial thin films, we recently studied the band structures of $\text{La}_{1-x}\text{Sr}_x\text{FeO}_3$ (LSFO) and $\text{La}_{1-x}\text{Sr}_x\text{MnO}_3$ (LSMO), and it has been demonstrated that *in-situ* ARPES measurements on such TM oxide films are one of the best methods to investigate the band structure of TM oxides with three-dimensional crystal

structures [8, 9].

In this paper, we report on analyses of ARPES results of bulk single crystals of SVO [3] and on *in-situ* ARPES results of single-crystal LSFO ($x = 0.4$) [9] and LSMO ($x = 0.4$) [8] thin films grown on SrTiO₃ (001) substrates. In the case of SVO, we have investigated the effect of surface on the ARPES spectra by comparing the experimental results with calculated surface electronic structures. The experimental band structures of LSFO and LSMO were interpreted using an empirical tight-binding band-structure calculation by assuming the G-type antiferromagnetic state for LSFO and the ferromagnetic state for LSMO. The mass enhancement compared with band-structure calculation is discussed in the case of SVO and LSMO. We also discuss the problem of intrinsic uncertainty in determining the momentum of electrons in the solid perpendicular to the crystal surface [10].

THEORETICAL ANALYSES

Tight-binding band-structure calculation

In the case of SVO, we adopted the simplest tight-binding (TB) model. In this simplest model, the t_{2g} bands are represented by a TB Hamiltonian with diagonal elements of the form

$$H_{xy,xy}(\mathbf{k}) = e_d + t_0(c_x + c_y) + t_1c_xc_y + [t_2 + t_3(c_x + c_y) + t_4c_xc_y]c_z, \quad (1)$$

where $c_i = 2 \cos(k_i a)$ ($i = x, y, z$) and a is the lattice constant [11]. Cyclic permutations yield $H_{yz,yz}(\mathbf{k})$ and $H_{zx,zx}(\mathbf{k})$. The t_i denote effective hopping integrals arising from the V-O-V hybridization. $t_{0,2}$, $t_{1,3}$, and t_4 specify the interaction between first, second, and third neighbors, respectively, and $|t_0| \gg |t_1|, |t_2|, |t_3|, |t_4|$. Off-diagonal elements which vanish at high-symmetry points are small and are neglected here.

In the case of LSFO and LSMO, we performed TB band-structure calculations explicitly including oxygen 2*p* orbitals for the three-dimensional perovskite structure in the antiferromagnetic (AF) and ferromagnetic (FM) states. TB calculations for the paramagnetic (PM) state were already reported in Refs. [12, 13, 14]. The size of the matrix for the latter calculation was 14×14 (TM 3*d* orbitals: 5, oxygen 2*p* orbitals: $3 \times 3 = 9$). As for LSFO, we performed the calculation assuming the G-type AF state, where all nearest-neighbor Fe

atoms have antiparallel spins. The effect of the G-type antiferromagnetism was treated phenomenologically by assuming an energy difference ΔE between the spin-up and spin-down Fe sites. As for LSMO, we performed the calculation assuming the FM state. The effect of ferromagnetism was again treated phenomenologically by assuming an energy difference ΔE between the spin-up and spin-down Mn sites. The size of the matrix to be diagonalized was 28×28 for LSFO (G-type AF), and 14×14 for LSMO (FM). Parameters to be adjusted are ΔE , the energy difference between the TM $3d$ level and the O $2p$ level $\epsilon_d - \epsilon_p$, and Slater-Koster parameters $(pd\sigma)$, $(pd\pi)$, $(pp\sigma)$, and $(pp\pi)$ [15]. Here, ϵ_d is the average of the majority-spin d -level $\epsilon_d - \Delta E/2$ and the minority-spin d -level $\epsilon_d + \Delta E/2$. The ratio $(pd\sigma)/(pd\pi)$ was fixed at -2.2 [16, 17], and $(pp\sigma)$ and $(pp\pi)$ were fixed at 0.60 eV and -0.15 eV, respectively. $(pd\sigma)$ is expected to be in the range of $-(1.4 - 1.9)$ eV for LSFO and near -1.8 eV for LSMO from a configuration-interaction (CI) cluster-model calculation reported in Refs. [18, 19]. Crystal-field splitting $10Dq$ of 0.41 eV was taken from Ref. [19]. Crystal-field splitting of O $2p$ orbitals is not taken into account. The TB basis functions used in the calculations of LSFO and LSMO are given in Tables I and III, and the matrix elements of the Hamiltonians for LSFO and LSMO are given in Tables II and IV, respectively.

Figure 1 shows the Brillouin zones (BZs) for the perovskite structure in the PM and FM states [(a)], the G-type AF state [(b)], and the G-type AF state with GdFeO_3 -type distortion [(c)]. The BZ of the FM state is the same as that of the PM state. The BZ of the G-type AF state is that of the face-centered cubic (fcc) lattice. In this paper, we will neglect the effect of the GdFeO_3 -type distortion and will only consider the effect of magnetic ordering.

Figure 2 shows schematic band structures along the Γ -X line obtained by TB calculation. Here, we have fixed $\epsilon_d - \epsilon_p - \Delta E/2$ at 3 eV. Panel (a) shows the band structure of the PM state calculated including only p - p interactions, namely, without p - d interaction ($(pd\sigma) = 0$). There are significant dispersions in the O $2p$ bands caused by the p - p interaction, whereas there are no dispersions in the e_g and t_{2g} bands, where there exists only the crystal-field splitting of $10Dq$. Panel (b) shows the band structure of the PM state calculated with $(pd\sigma) = -2.0$ eV. The e_g and t_{2g} bands now become dispersive due to the p - d interaction. Panels (c) and (d) show the band structure of the FM and G-type AF states, respectively. The values of ΔE were taken as 5.0 eV in both cases. In the FM state, since $\epsilon_d - \epsilon_p - \Delta E/2$ is fixed, the up-spin (majority-spin) e_g and t_{2g} bands do not change appreciably compared with those in the PM state, whereas the down-spin (minority-spin) e_g and t_{2g} bands are pushed

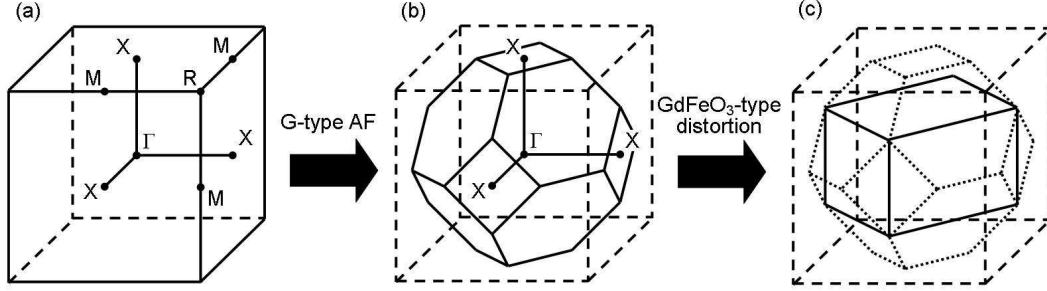


FIG. 1: Brillouin zones of the perovskite structure. (a)PM and FM states. (b)G-type AF state. Broken lines represent the BZ of the PM state. (c)G-type AF state with GdFeO₃-type distortion. Broken lines and dotted lines represent the BZs of the PM state and the G-type AF state, respectively.

up by ΔE (out of the range of Fig. 2 (c)). In the G-type AF state, band dispersions along the R-M line are folded onto the Γ -X line, and hybridization between these bands causes a maximum in the e_g bands in the middle of Γ and X.

k_z broadening

In ARPES measurements, there is an intrinsic uncertainty in the momentum of electrons in the solid perpendicular to the crystal surface due to a finite escape depth λ of photoelectrons [10]. Here, the z -axis is taken as the direction perpendicular to the surface toward the vacuum side. Inside the solid ($z < 0$) the wave function of an emitted photoelectron with a wave number k_{z0} is approximated by

$$\psi(z) = \frac{1}{\sqrt{\lambda}} \exp(ik_{z0}z) \exp(z/2\lambda), \quad (2)$$

where λ denotes the escape depth of a photoelectron. $|\psi(z)|^2 = \exp(z/\lambda)/\lambda$ shows an exponential decay of photoelectrons within the solid. The Fourier transform of Eq. (2), $\phi(k_z)$, is

$$\phi(k_z) \propto \frac{1}{i(k_z - k_{z0}) - 1/2\lambda}. \quad (3)$$

and $|\phi(k_z)|^2$ becomes proportional to

$$L(k_z) = \frac{1}{2\pi\lambda} \frac{1}{(k_z - k_{z0})^2 + (1/2\lambda)^2}, \quad (4)$$

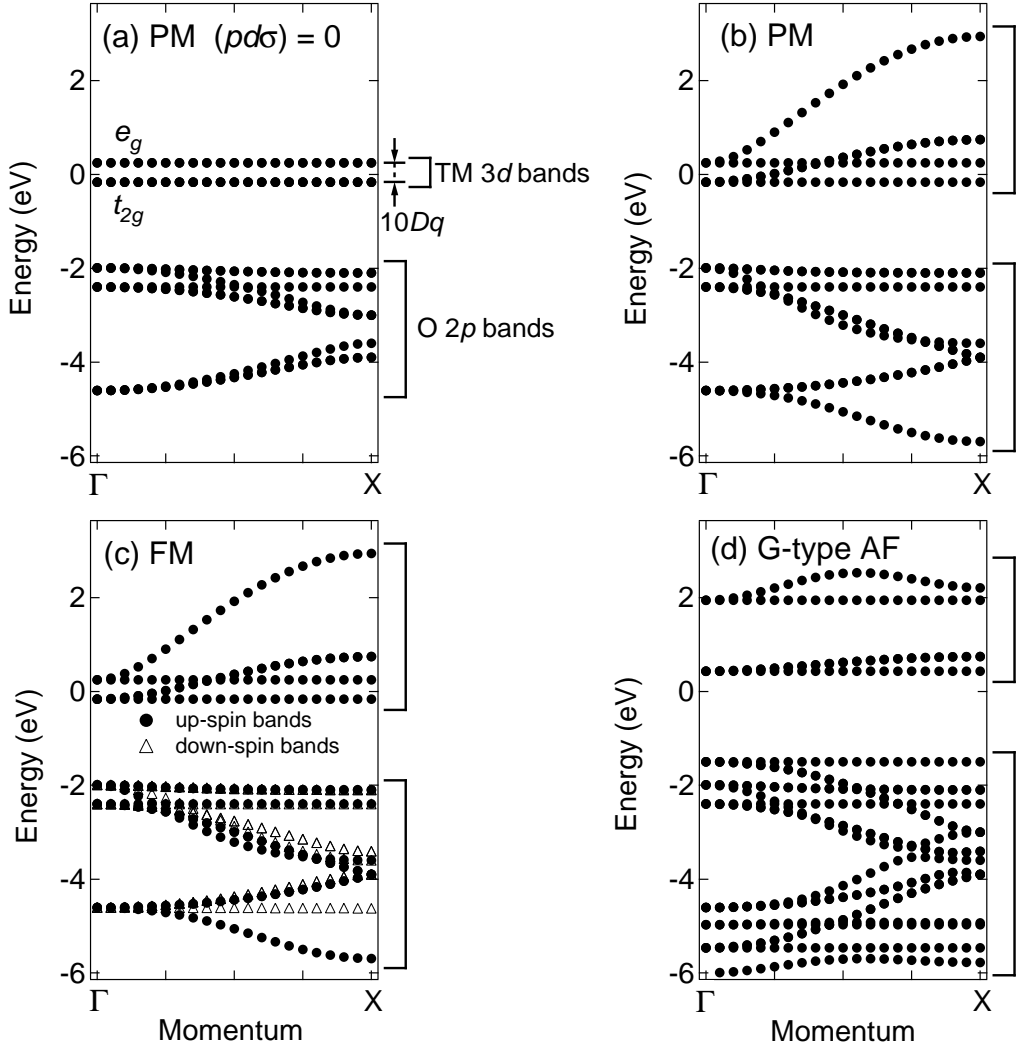


FIG. 2: Band structures obtained by TB calculation. $\epsilon_d - \epsilon_p - \Delta E/2 = 3$ eV has been fixed. (a)PM state with only p - p interaction included ($(pd\sigma) = 0$). (b)PM state with $(pd\sigma) = -2.0$ eV. (c)FM state with $\Delta E = 5.0$ eV. (d)G-type AF state with $\Delta E = 5.0$ eV.

which means that the intrinsic uncertainty of k_z is given by the Lorentzian function with the full width at half maximum of $1/\lambda$.

The effect of the k_z broadening is very important for the interpretation of ARPES results. For example, we consider an isotropic band with the bottom at the Γ point, expressed as

$$E = \alpha(k_x^2 + k_y^2 + k_z^2). \quad (5)$$

If we measure photoelectrons with momentum $\vec{K} = (K_x, K_y, K_z)$, where K_z is related to k_z

through the momentum conservation $k_x = K_x$ and $k_y = K_y$ and the energy conservation, the obtained spectrum becomes,

$$D(k_x, k_y, E) = \int_{-\infty}^{\infty} dk_z L(k_z) \delta(E - \alpha(k_x^2 + k_y^2 + k_z^2)). \quad (6)$$

From Eq. (4) and using the identity

$$\delta(x - \alpha k_z^2) = \frac{1}{2\sqrt{\alpha x}} \left[\delta\left(k_z - \sqrt{\frac{x}{\alpha}}\right) + \delta\left(k_z + \sqrt{\frac{x}{\alpha}}\right) \right], \quad (7)$$

we obtain

$$D(k_x, k_y, E) = \frac{1}{4\pi\lambda\sqrt{\alpha\{E - \alpha(k_x^2 + k_y^2)\}}} \times \left[\frac{1}{\left(\frac{\sqrt{\{E - \alpha(k_x^2 + k_y^2)\}}}{\alpha} - k_{z0}\right)^2 + (1/2\lambda)^2} + \frac{1}{\left(\frac{\sqrt{\{E - \alpha(k_x^2 + k_y^2)\}}}{\alpha} + k_{z0}\right)^2 + (1/2\lambda)^2} \right]. \quad (8)$$

We plot the function $D(k_x, k_y, E)$ with $k_x = k_y = 0$ for various values of λ in Fig. 3. Here, we have assumed that $\alpha = 8 \text{ eV}\cdot\text{\AA}^2$, which corresponds to $m^* \sim 0.5m_e$ (m^* is an effective band mass and m_e is the electron mass in vacuum), and $k_{z0} = \pi/4c$, where $c = 3.830 \text{ \AA}$, the out-of-plane lattice constant of LSMO ($x = 0.4$) thin films. One can see that in bulk-sensitive measurements using high-energy photons, like $\lambda = 20 \text{ \AA}$, there is a peak at $E = \alpha k_{z0}^2$. In contrast, in surface-sensitive measurements using low-energy photons, there is no peak at αk_{z0}^2 but $D(E)$ is peaked around $E \sim 0$. The density of states at the Γ point is very large because the band has a van Hove singularity at this point. Since bands usually have van Hove singularities along a high-symmetry line, the effect of k_z broadening is very important when we trace near the high-symmetry line using low energy photons. Our photon energies used in the ARPES measurements were in the range of $20 - 100 \text{ eV}$ and therefore $\lambda \sim 5 \text{ \AA}$, meaning that considering the k_z -broadening effect is crucial in the interpretation of ARPES results.

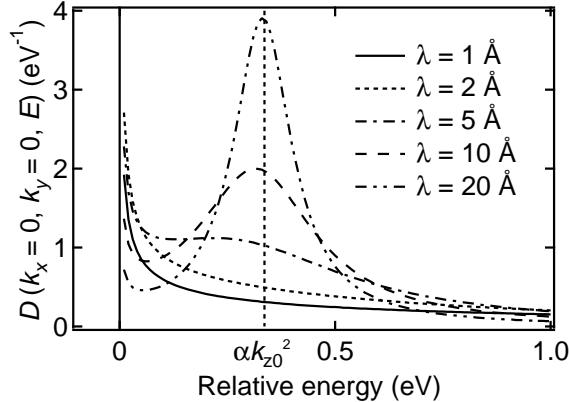


FIG. 3: ARPES spectrum $D(k_x, k_y, E)$ with $k_x = k_y = 0$ for various values of escape depths of photoelectrons λ .

RESULTS AND DISCUSSION

SrVO₃

SVO is an ideal system to study the fundamental physics of electron correlation because it is a prototypical Mott-Hubbard-type with d^1 electron configuration. For the bandwidth-control system $\text{Ca}_{1-x}\text{Sr}_x\text{VO}_3$ (CSVO), the existence and the extent of effective mass enhancement and spectral weight transfer have been quite controversial. Early photoemission results have shown that, with decreasing x , i.e., with decreasing bandwidth, spectral weight is transferred from the coherent part to the incoherent part [20] in a more dramatic way than the enhancement of the electronic specific heats γ [21]. In contrast, in a recent bulk-sensitive photoemission study using soft x rays it was claimed that there was no appreciable spectral weight transfer between SrVO₃ and CaVO₃ [22].

ARPES measurements on SVO were performed at beamline 5-4 of Stanford Synchrotron Radiation Laboratory (SSRL). Bulk single crystals of SVO were grown using the traveling-solvent floating zone method. Samples were first aligned *ex situ* using Laue diffraction, cleaved *in situ* along the cubic (100) surface at a temperature of 15 K and measured at the same temperature. Details of the experimental conditions of ARPES are described in Ref. [3].

An example of ARPES spectra for SVO near E_F are shown in Fig. 4. The coherent part within ~ 0.7 eV of E_F shows a parabolic energy dispersion, consistent with the view that

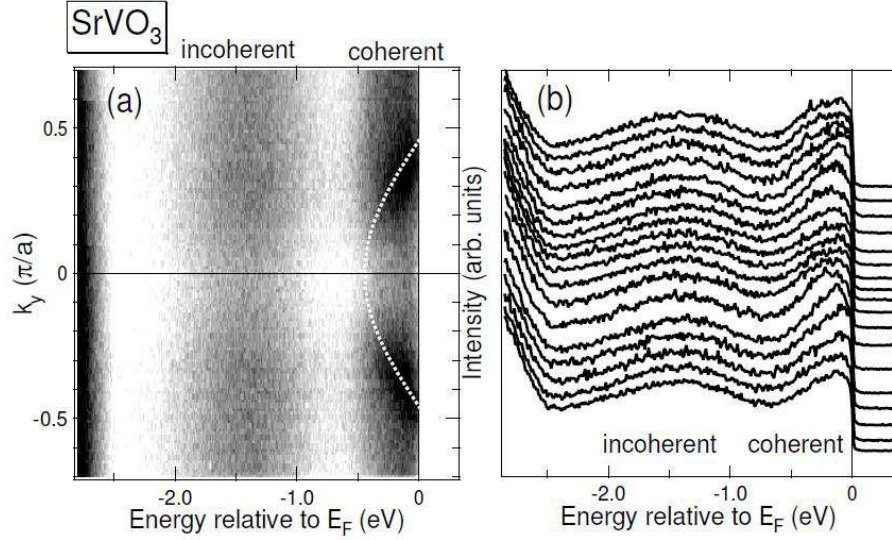


FIG. 4: ARPES spectra of SrVO₃ along momentum cut 2 in the Brillouin zone shown in Fig. 5. (a) Intensity plot in the $E-k_y$ plane. Dispersive feature within ~ 0.7 eV of E_F is the coherent part, while a broad feature around -1.5 eV is the incoherent part. (b) Energy distribution curves (EDC's).

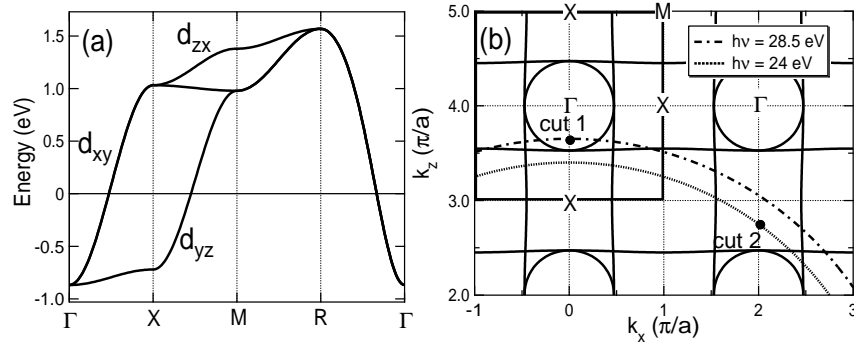


FIG. 5: Band structure and the Fermi surface of SrVO₃. (a) Band dispersions obtained by local-density approximation (LDA) band-structure calculation [23]. (b) $k_y=0$ cross-sectional view of the Fermi surfaces and the momentum loci corresponding to the mapping in Fig. 6.

the coherent part corresponds to the calculated band structure. On the other hand, the incoherent part centered at ~ -1.5 eV does not show an appreciable dispersion but shows a slight modulation of the intensity, which coincides with that of the coherent part, as seen in Fig 4(a). To compare with the band-structure calculation, we shall focus on the dispersive feature of the coherent part.

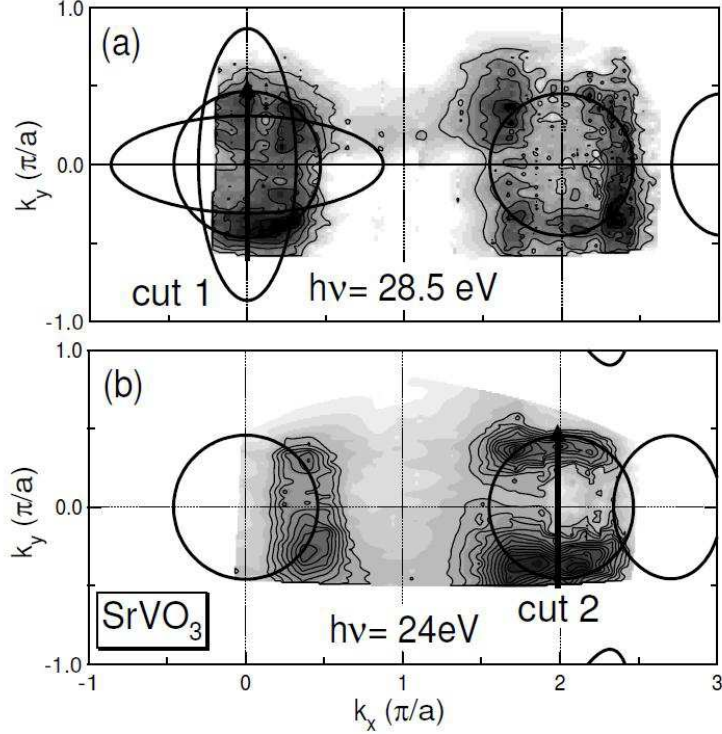


FIG. 6: Spectral weight mapping at E_F for SrVO_3 . (a) Mapping with $h\nu=28.5\text{eV}$. (b) Mapping with $h\nu=24\text{eV}$. Note that the mapping is projection on the k_x - k_y plane.

The band dispersions obtained by local-density approximation (LDA) band-calculation [23] are shown in Fig. 5 (a). The hopping parameters of the TB model (1) have been obtained by fitting the TB bands to the results of LDA band-structure calculation [23]. Figure 5 (b) illustrates the $k_y=0$ cross-sectional view of the Fermi surfaces expressed by the TB model. The three bands correspond to the d_{xy} , d_{yz} and d_{zx} orbitals of V and scarcely hybridize with each other. Therefore, these dispersions are almost two-dimensional and form three cylindrical Fermi surfaces intersecting each other around the Γ point, although the crystal structure is three-dimensional. The loci of electron momenta in the k_x - k_z plane for constant photon energies $h\nu=24\text{eV}$ and 28.5eV are plotted in Fig. 5(b). Here, the inner potential of 10eV has been assumed.

Figure 6 (a) and (b) shows spectral weight mapping in the k_x - k_y space at E_F on the momentum loci for the photon energies $h\nu=28.5$ and 24eV , respectively. The spectral weight for both photon energies are largely confined within the cylindrical Fermi surfaces extended in the k_z direction. According to Fig.5(b), cut 2 corresponds to momenta near the X point [$\mathbf{k} = (1,0,0)$]. Therefore, the observed spectral weight comes only from one

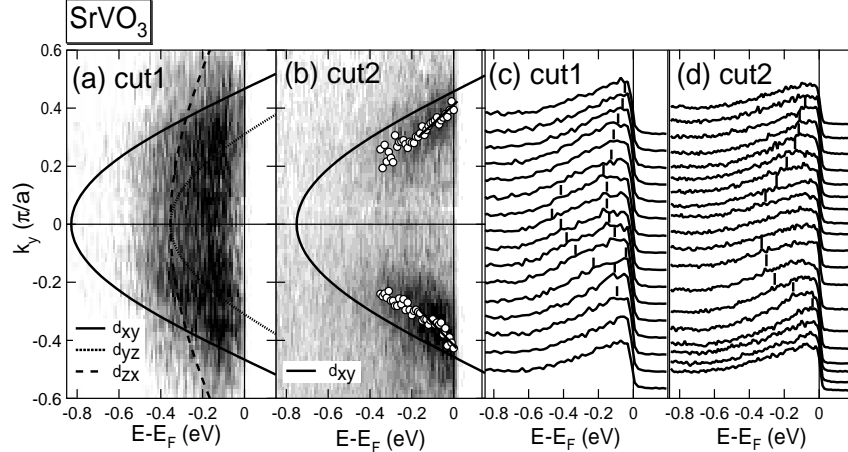


FIG. 7: ARPES spectra of SrVO₃ for cuts 1 and 2 in Fig. 5. Panels (a) and (b) show intensity plots in E - k space for cuts 1 and cut 2, respectively. Angle-independent backgrounds have been subtracted. Calculated TB band are also superimposed. Circles in (b) are peak positions of MDC's and represents band dispersion. Panels (c) and (d) are EDC's corresponding to panels (a) and (b), respectively. Vertical bars are guides to the eye indicating the positions of the dispersive features.

cylindrical Fermi surface referred to as the γ sheet [24], which arises from the d_{xy} orbital. On the other hand, the spectral weight in the first BZ for $h\nu = 28.5$ eV (cut 1) is enclosed by the three cylindrical Fermi surfaces [24]. Indeed, EDC's along cut 1 [Fig. 7 (c)] show complicated features suggestive of two energy dispersions.

Figure 7(a) and (b) show intensity plots in the energy-momentum (E - k) space corresponding to each cut in Fig. 5. The E - k_y plots are compared with the energy dispersions expected from the LDA calculation [23]. Figure 7(c) and (d) show EDC's corresponding to panels (a) and (b), respectively. The EDC's of cut 1 in panel (c) show parabolic energy dispersions with the bottom at ~ -0.5 eV, shallower than that expected from the LDA calculation ~ -0.9 eV. Since the momenta of cut 1 are within the α and β sheets of the Fermi surface, there are two dispersions. These dispersions may correspond to the dispersions of the d_{xy} and d_{yz} bands. The dispersion of d_{zx} is not clearly observed in the present plot, probably due to the effect of transition matrix-elements.

For cut 2 [Fig. 7 (b) and (d)], since it does not intersect the d_{yz} and d_{zx} bands, only the d_{xy} band are observed. In panel (b), we have derived the band dispersion for cut 2 from MDC peak positions indicated by circles. By comparing the Fermi velocity of the LDA band structure and that of the present experiment, one can see an overall band narrowing

in the measured band dispersion. Near E_F , we obtain the mass enhancement factor of $m^*/m_b \sim 1.8 \pm 0.2$, which is close to the value $m^*/m_b = 1.98$ obtained from the specific heat coefficient γ [21]. Since the LDA calculation predicted that the d_{xy} band is highly two-dimensional and nearly isotropic within the k_x - k_y plane, a similar mass enhancement is expected on the entire Fermi surface.

It has been pointed out that the photoemission spectra of SVO taken at low photon energies have a significant amount of contributions from surface states, particularly in the incoherent part [22, 25]. In order to distinguish bulk from surface contributions in the present spectra, we consider the character of surface states created by the discontinuity of the potential at the surfaces. According to a tight-binding Green's function formalism for a semi-infinite system [11, 26], surface-projected density of states of surface-parallel d_{xy} band and surface-perpendicular $d_{yz,zx}$ band have different nature. The surface d_{xy} band does not show an appreciable change from the bulk band because it has the two-dimensional character within the x - y plane. In contrast, spectral weight of the surface $d_{yz,zx}$ states is redistributed between the bulk $d_{yz,zx}$ band and the Fermi level [3], because k_z is no longer a good quantum number. This leads to the absence of clear dispersions of the surface $d_{yz,zx}$ bands in ARPES as demonstrated in Ref. [3]. Accordingly, the observed dispersion of the d_{xy} band should represent that of the bulk d_{xy} band.

La_{1-x}Sr_xFeO₃

LSFO undergoes a pronounced charge disproportionation and an associated MIT around $x \sim 2/3$ [27]. One striking feature of LSFO is that the insulating phase is unusually wide in the phase diagram ($0 < x < 0.5$ at room temperature and even $0 < x < 0.7$ at low temperatures) [28]. In a previous photoemission study, the gap at the Fermi level (E_F) was observed for all compositions for $0 \leq x \leq 0.67$ [19], consistent with the wide insulating region of this system.

ARPES measurements on LSFO were carried out using a photoemission spectroscopy (PES) system combined with a laser molecular beam epitaxy (MBE) chamber, which was installed at beamline BL-1C of Photon Factory, KEK [6]. The preparation and characterization of the LSFO films are described in Ref. [19]. By low energy electron diffraction (LEED), sharp 1×1 spots were observed with no sign of surface reconstruction, confirming

the well-ordered surfaces of the films. Details of the experimental conditions are described in Ref. [9].

The left panel of Fig. 8 (a) shows a gray-scale plot of the experimental band structure obtained by ARPES measurements of an LSFO ($x = 0.4$) thin film with the photon energy of 74 eV [9]. Here, the second derivatives of the EDC's are plotted on the gray scale, where dark parts correspond to energy bands. In Fig. 8 (b), hole pockets obtained by a TB calculation (described below) are also shown. The trace obtained for $h\nu = 74$ eV crosses the calculated hole pocket. The structure at -1.3 eV shows a significant dispersion, and is assigned to the Fe $3d$ majority-spin e_g bands. The structure at -2.4 eV shows a weaker dispersion than the e_g bands, and is assigned to the Fe $3d$ t_{2g} majority-spin bands. The structures at $-(4 - 7)$ eV are assigned to the O $2p$ bands. The e_g bands do not cross E_F , consistent with the insulating behavior and the persistence of the gap observed in the angle-integrated PES (AIPES) spectra [19].

The best fit of TB calculation [right panel of Fig. 8 (a)] to the observed band dispersions and the optical gap of 2.1 eV of LaFeO₃ (LFO) [29] has been obtained with $\epsilon_d - \epsilon_p = 2.65$ eV, $(pd\sigma) = -1.5$ eV, and $\Delta E = 5.3$ eV. We also considered the effect of k_z broadening given by a Lorentzian function as described in Sec. 2.2. Here we have used the value $\lambda = 5$ Å. $\Delta k_z \sim 1/\lambda$ (~ 0.2 Å⁻¹) is approximately 10 % of the Brillouin zone ($2\pi/a$). Here, it should be noted that $\epsilon_d - \epsilon_p$, $(pd\sigma)$ and ΔE primarily determine the Fe $3d - O$ $2p$ band positions, their dispersions, and the optical band gap, respectively. The dispersions of the e_g bands were successfully reproduced. The very weak dispersions of the t_{2g} bands and the width of the O $2p$ bands were also well reproduced by this calculation. The energy position of the calculated E_F determined from the filling of electrons was not in agreement with the experimental E_F , however. This discrepancy corresponds to the fact that this material is insulating up to 70 % hole doping while the rigid-band model based on the band-structure calculation gives the metallic state.

La_{1-x}Sr_xMnO₃

LSMO has been attracting great interest because of its intriguing properties, such as the CMR effect [30] and half metallic nature [31]. One end member of LSMO, LaMnO₃, is an antiferromagnetic insulator, and hole-doping induced by the substitution of Sr for La

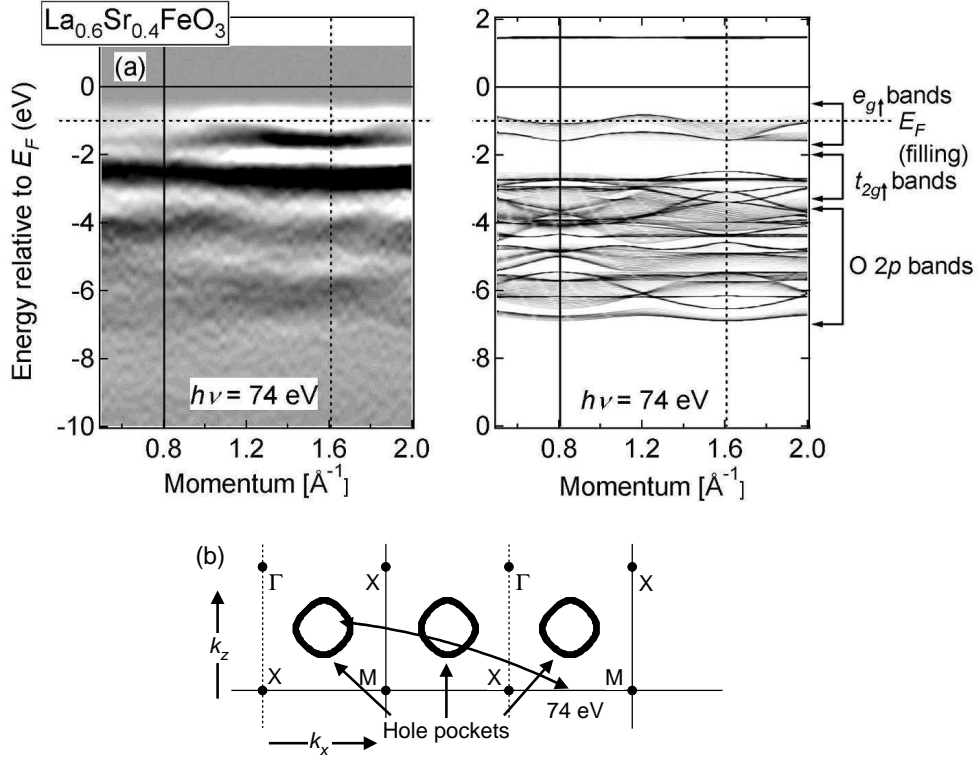


FIG. 8: Comparison of ARPES spectra of an LSFO thin film taken at $h\nu = 74$ eV with TB calculation. The left panel of (a) shows the experimental band structure (dark parts correspond to energy bands) and the right panel of (a) shows the result of TB calculation. The traces in k -space and calculated hole pockets are shown in (b).

produces a ferromagnetic metallic phase ($0.17 < x < 0.5$) [30].

ARPES measurements on LSMO were carried out using the same system as in the case of LSFO. The preparation and characterization of the LSMO films are described in Refs. [32]. The surface structure and cleanliness of the films were checked by LEED. Some surface reconstruction-derived spots were observed in addition to sharp 1×1 spots, confirming the well-ordered surfaces of the films, but surface reconstruction is expected to affect the obtained band dispersions. Details of the experimental conditions are described in Ref. [8].

The left panel of Fig. 9 (a) shows a gray-scale plot of the experimental band structure obtained by ARPES measurements of an LSMO ($x = 0.4$) thin film with the photon energy of 88 eV [8]. Here, the second derivatives of the EDC's are plotted on the gray scale, where dark parts correspond to energy bands as in the case of LSFO along the trace in k -space

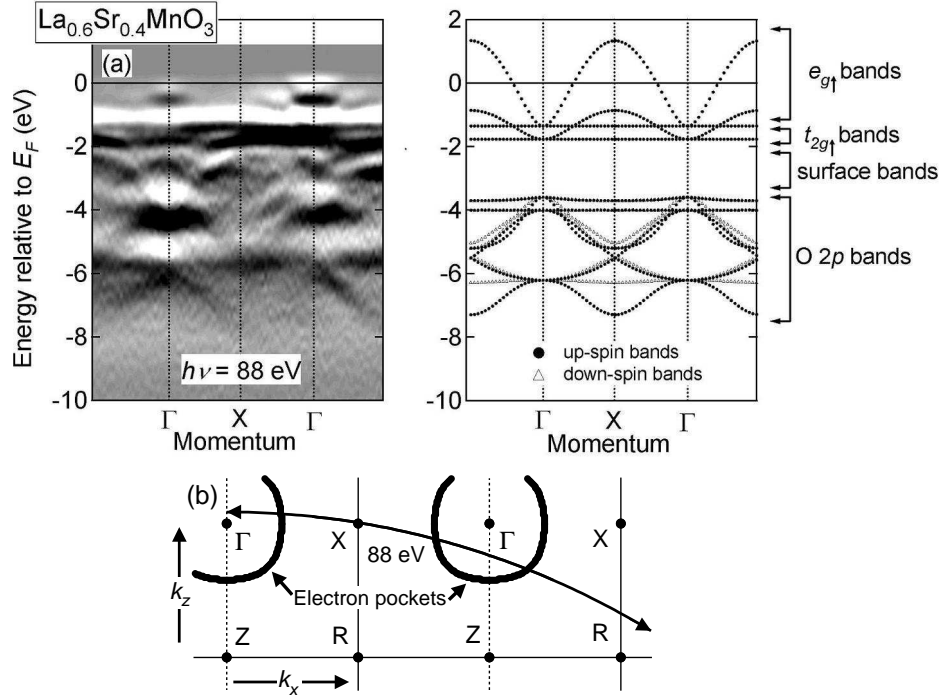


FIG. 9: Comparison of ARPES spectra of an LSMO thin film taken at $h\nu = 88$ eV and TB calculation. The left panel of (a) shows the experimental band structure (dark parts correspond to energy bands) [8] and the right panel of (a) shows the result of TB calculation. The traces in k -space and calculated electron pockets are shown in (b).

shown in Fig. 9 (b). Note that this trace is approximately along the Γ -X direction. We shall assume that the trace is exactly along the Γ -X direction for the moment. The effect of the deviation from the Γ -X line will be discussed below. Here, electron pockets obtained by a TB calculation are also shown in Fig. 9 (b). One of the Mn $3d$ majority-spin e_g bands at $-(0-1)$ eV shows a significant dispersion and crosses E_F , corresponding to the half metallic behavior [31]. The E_F crossing of the e_g bands is consistent with the observed Fermi edge in the AIPES spectra [32]. The Mn $3d$ majority-spin t_{2g} bands at $-(1-2)$ eV show weaker dispersions than the e_g bands. The bands at $-(2-3)$ eV shows dispersions with a shorter period in k -space than the Brillouin zone. This means that these bands are affected by the surface reconstruction detected in the LEED pattern. The O $2p$ bands are located at $-(4-7)$ eV.

The best fit of the TB calculation to the observed band dispersions [right panel of Fig. 9 (a)] has been obtained with $\epsilon_d - \epsilon_p = 5.3$ eV, $(pd\sigma) = -2.0$ eV, and $\Delta E = 4.6$ eV. The

strong dispersions of the e_g bands, the weak dispersions of the t_{2g} bands, and the width of the O $2p$ bands were successfully reproduced, although there are no bands in the calculation corresponding to the experimental surface bands. The bottom of the e_g bands is at ~ -0.5 eV in the experiment and at ~ -1.5 eV in the calculation. This difference may come from the mass renormalization caused by strong electron correlation in this system. One can estimate the mass enhancement to be $m^*/m_b \sim 2.5$.

Figure 10 (a) shows the calculated density of states (DOS) of the FM state. The partial DOS's for the majority-spin Mn e_g , the majority-spin Mn t_{2g} , the minority-spin Mn e_g , and the minority-spin Mn t_{2g} orbitals are shown in the lower panels. No band gap opens between the majority-spin e_g bands and the minority-spin t_{2g} bands for the present ΔE value. In Fig. 10 (a), the E_F position has been determined from the filling of electrons, and also calculated DOS at E_F [$D^b(E_F)$] has been obtained. Using the relationship

$$\gamma^b = \frac{\pi^2}{3} k_B^2 D^b(E_F), \quad (9)$$

we obtain the calculated electronic specific heat coefficient by $\gamma^b \sim 1$ [mJ mol² K⁻²]. The experimental electronic specific heat coefficient has been reported as $\gamma \sim 3.5$ [mJ mol² K⁻²] [33]. Thus $m^*/m_b = \gamma/\gamma_b \sim 3.5$, in fairly good agreement with $m^*/m_b \sim 2.5$ derived from ARPES, which means that effective mass m^* is renormalized as

$$m^*/m_b \sim 2.5 - 3.5. \quad (10)$$

Figure 10 (b) shows the comparison of the chemical potential shift obtained from the TB calculation in the FM region of LSMO ($0.2 \leq x \leq 0.4$ [30, 32]) within the rigid-band model (i.e., assuming the constant exchange splitting) and that determined experimentally from core-level photoemission spectra [32]. The experimental chemical potential shift is slower than the calculated one by a factor of ~ 0.4 , which means

$$\frac{\partial \mu}{\partial n} \sim \frac{0.4}{D^b(E_F)}. \quad (11)$$

For a metallic system, the rigid-band picture predicts that

$$\frac{\partial \mu}{\partial n} = \frac{1+F}{D^*(E_F)} = \left(\frac{m_b}{m^*}\right) \frac{1+F}{D^b(E_F)}, \quad (12)$$

where $D^*(E_F)$ is the DOS of renormalized quasiparticles (QPs) and F is a parameter which represents the effective QP-QP repulsion. From Eqs. (10)-(12), one obtains $F \sim 0 - 0.4$.

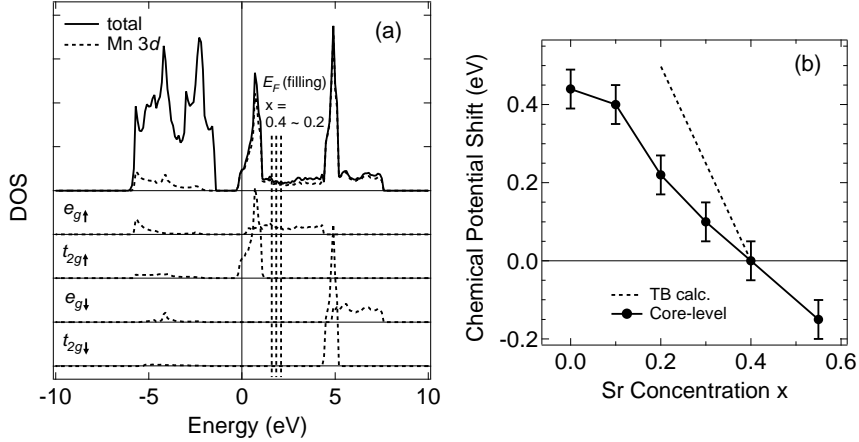


FIG. 10: Chemical potential shift in LSMO. (a) DOS obtained from TB calculation. (b) Comparison of the chemical potential shift calculated for the rigid-band-model using TB calculation and that determined experimentally from core-level photoemission spectra [32].

This value is much smaller than the values of F_0^s in AF compounds. For example, it was reported that $F_0^s \sim 7$ for $\text{La}_{2-x}\text{Sr}_x\text{CuO}_4$, and ~ 6 for $\text{La}_{1-x}\text{Sr}_x\text{VO}_3$ [34]. In the FM case, one obtains small values of F compared to the AF case, probably because of the strong exchange interaction between carriers in the FM case.

Now we go back to the effect of the deviation of the trace with $h\nu = 88$ eV from the Γ -X direction. Figure 11 shows a TB simulation of the ARPES spectra of LSMO taken at 88 eV using the above-mentioned parameter values. Panels (a), (b) and (c) show the results for $\Delta k_z = 0$ (without k_z broadening), $\Delta k_z = 1/\lambda$, and $\Delta k_z = \infty$ (uniform integration in k_z), respectively. In panel (a), the energy position of the bottom of the e_g bands at $k_{\parallel} = 0 \text{ \AA}^{-1}$ is different from that at $k_{\parallel} = 1.6 \text{ \AA}^{-1}$, while in panel (b) the bottoms are at almost the same energy positions. In experiment [Fig. 9 (a)], the bottoms are almost at the same energy positions, which means that the experimental results are in good agreement with (b), that is $\Delta k_z = 1/\lambda$. In panel (c), there are two bands approaching E_F , in disagreement with experiment.

Figure 12 shows comparison of the dispersion along the Γ -X direction (dots) and simulated spectra (gray scale) obtained assuming $\Delta k_z = 1/\lambda$ for $h\nu = 88$ eV. There are some discrepancies in the high-binding-energy region $-(4 - 7)$ eV, but the overall agreement is rather good in the region near E_F $[-(0 - 2)$ eV]. This means that one can trace the band

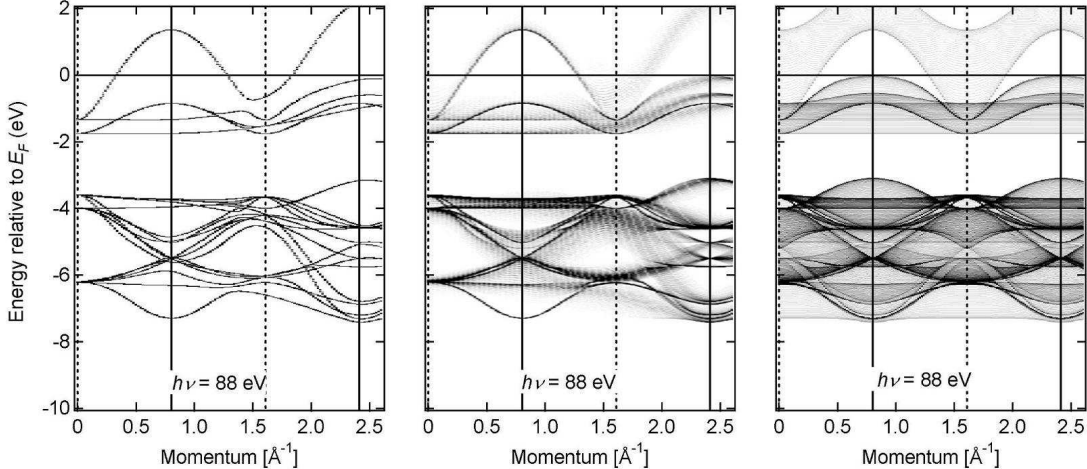


FIG. 11: Simulated ARPES spectra of LSMO ($x = 0.4$) taken at 88 eV on TB calculation. (a) $\Delta k_z = 0$, (b) $\Delta k_z = 1/\lambda$, (c) $\Delta k_z = \infty$.

dispersions almost along the Γ -X direction by performing ARPES with a fixed photon energy of $h\nu = 88$ eV because of the large k_z -integrated DOS at a high-symmetry line (in this case the Γ -X direction). Even if the trace somewhat deviates from a high-symmetry line, one can trace the dispersion along the high-symmetry line due to the large DOS and the effect of k_z broadening. By changing the photon energy with changing the emission angle in ARPES measurements, one can map band dispersions precisely along the Γ -X line. However, the photoionization cross section varies with a photon energy, making the interpretation difficult. In practice, fixing a photon energy and changing an emission angle is a more efficient and useful way to obtain band dispersions in such materials. We also revealed that considering the effect of k_z broadening is important for the interpretation of the ARPES of the three-dimensional materials.

CONCLUSION

We have analyzed the ARPES data of SVO bulk crystals and LSFO ($x = 0.4$) and LSMO ($x = 0.4$) thin films using TB band-structure calculations. As for SVO, the enhanced effective electron mass obtained from the energy band near E_F was consistent with the bulk thermodynamic properties. The experimental band structures of LSFO and LSMO were interpreted using a TB band-structure calculation. The overall agreement between

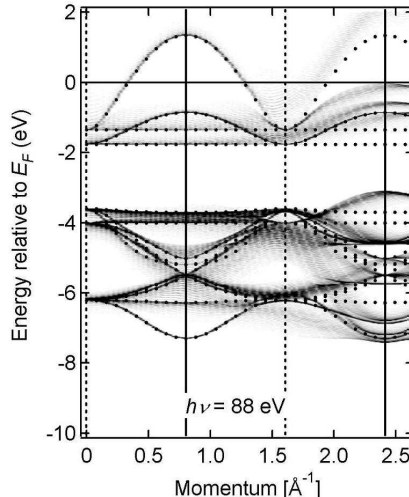


FIG. 12: Comparison of the dispersion along the Γ -X direction (dots) and simulated spectra (gray scale) for LSMO ($x = 0.4$) calculated assuming $\Delta k_z = 1/\lambda$ at 88 eV.

experiment and calculation is fairly good. However, in the case of LSFO, the energy position of the calculated E_F was not in agreement with the experimental E_F , reflecting the insulating behavior. In the case of LSMO, experimental energy bands were narrowed compared with calculation due to strong electron correlation. We also demonstrated that considering the effect of k_z broadening is important for the interpretation of the ARPES results of such three-dimensional materials.

Acknowledgments

This work was supported by a Grant-in-Aid for Scientific Research No. A16204024 from the Japan Society for the Promotion of Science (JSPS) and “Invention of Anomalous Quantum Materials” No. 16076208 from the Ministry of Education, Culture, Sports, Science and Technology, Japan. The authors are grateful to D. H. Lu for technical support at SSRL. SSRL is operated by the Department of Energy’s Office of Basic Energy Science, Division of Chemical Sciences and Material Sciences. Part of this work was done under the approval of the Photon Factory Program Advisory Committee under Project No. 2002S2-002 at the Institute of Material Structure Science, KEK. H.W. acknowledges financial support from JSPS.

**BASIS FUNCTIONS AND MATRIX ELEMENTS FOR TB BAND-STRUCTURE
CALCULATIONS**

TABLE I: TB basis functions used in the band-structure calculation of LSFO

	No.	Origin	Function	No.	Origin	Function
Fe $3d$	1	(0, 0, 0)	xy	15	$a(1, 0, 0)$	xy
	2	(0, 0, 0)	yz	16	$a(1, 0, 0)$	yz
	3	(0, 0, 0)	zx	17	$a(1, 0, 0)$	zx
	4	(0, 0, 0)	$3z^2 - r^2$	18	$a(1, 0, 0)$	$3z^2 - r^2$
	5	(0, 0, 0)	$x^2 - y^2$	19	$a(1, 0, 0)$	$x^2 - y^2$
O $2p$	6	$\frac{1}{2}a(1, 0, 0)$	x	20	$\frac{1}{2}a(3, 0, 0)$	x
	7	$\frac{1}{2}a(1, 0, 0)$	y	21	$\frac{1}{2}a(3, 0, 0)$	y
	8	$\frac{1}{2}a(1, 0, 0)$	z	22	$\frac{1}{2}a(3, 0, 0)$	z
	9	$\frac{1}{2}a(0, 1, 0)$	x	23	$\frac{1}{2}a(2, 1, 0)$	x
	10	$\frac{1}{2}a(0, 1, 0)$	y	24	$\frac{1}{2}a(2, 1, 0)$	y
	11	$\frac{1}{2}a(0, 1, 0)$	z	25	$\frac{1}{2}a(2, 1, 0)$	z
	12	$\frac{1}{2}a(0, 0, 1)$	x	26	$\frac{1}{2}a(2, 0, 1)$	x
	13	$\frac{1}{2}a(0, 0, 1)$	y	27	$\frac{1}{2}a(2, 0, 1)$	y
	14	$\frac{1}{2}a(0, 0, 1)$	z	28	$\frac{1}{2}a(2, 0, 1)$	z

TABLE II: Nonzero matrix elements of the TB Hamiltonian used in the calculation of LSFO. $\xi \equiv k_x a$, $\eta \equiv k_y a$, and $\zeta \equiv k_z a$.

A. d - d interactions

$$\begin{aligned}
 H_{1,1} = H_{2,2} = H_{3,3} &= \epsilon_d - 4Dq - \Delta E/2, & H_{4,4} = H_{5,5} &= \epsilon_d + 6Dq - \Delta E/2 \\
 H_{15,15} = H_{16,16} = H_{17,17} &= \epsilon_d - 4Dq + \Delta E/2, & H_{18,18} = H_{19,19} &= \epsilon_d + 6Dq + \Delta E/2
 \end{aligned}$$

B. p - p interactions

$$C_1 = \frac{1}{2}(pp\sigma) + \frac{1}{2}(pp\pi), C_2 = \frac{1}{2}(pp\sigma) - \frac{1}{2}(pp\pi), C_3 = (pp\pi)$$

$$H_{6,6} = H_{10,10} = H_{14,14} = H_{20,20} = H_{24,24} = H_{28,28} = \epsilon_p$$

$$H_{7,7} = H_{8,8} = H_{9,9} = H_{11,11} = H_{12,12} = H_{13,13} = \epsilon_p$$

$$H_{21,21} = H_{22,22} = H_{23,23} = H_{25,25} = H_{26,26} = H_{27,27} = \epsilon_p$$

$$H_{6,9} = H_{7,10} = H_{20,23} = H_{21,24} = 2C_1 \cos\left(\frac{1}{2}\xi - \frac{1}{2}\eta\right)$$

$$H_{6,10} = H_{7,9} = H_{20,24} = H_{21,23} = -2C_2 \cos\left(\frac{1}{2}\xi - \frac{1}{2}\eta\right)$$

$$H_{6,12} = H_{8,14} = H_{20,26} = H_{22,28} = 2C_1 \cos\left(\frac{1}{2}\xi - \frac{1}{2}\zeta\right)$$

$$H_{6,14} = H_{8,12} = H_{20,28} = H_{22,26} = -2C_2 \cos\left(\frac{1}{2}\xi - \frac{1}{2}\zeta\right)$$

$$H_{6,23} = H_{7,24} = H_{20,9} = H_{21,10} = 2C_1 \cos\left(\frac{1}{2}\xi + \frac{1}{2}\eta\right)$$

$$H_{6,24} = H_{7,23} = H_{20,10} = H_{21,9} = 2C_2 \cos\left(\frac{1}{2}\xi + \frac{1}{2}\eta\right)$$

$$H_{6,26} = H_{8,28} = H_{20,12} = H_{22,14} = 2C_1 \cos\left(\frac{1}{2}\xi + \frac{1}{2}\zeta\right)$$

$$H_{6,28} = H_{8,26} = H_{20,14} = H_{22,12} = 2C_2 \cos\left(\frac{1}{2}\xi + \frac{1}{2}\zeta\right)$$

$$H_{7,13} = H_{21,27} = 2C_3 \cos\left(\frac{1}{2}\xi - \frac{1}{2}\zeta\right)$$

$$H_{7,27} = H_{21,13} = 2C_3 \cos\left(\frac{1}{2}\xi + \frac{1}{2}\zeta\right)$$

$$H_{8,11} = H_{22,25} = 2C_3 \cos\left(\frac{1}{2}\xi - \frac{1}{2}\eta\right)$$

$$H_{8,25} = H_{22,11} = 2C_3 \cos\left(\frac{1}{2}\xi + \frac{1}{2}\eta\right)$$

$$H_{9,12} = H_{23,26} = 2C_3 \cos\left(\frac{1}{2}\eta - \frac{1}{2}\zeta\right)$$

$$H_{9,26} = H_{23,12} = 2C_3 \cos\left(\frac{1}{2}\eta + \frac{1}{2}\zeta\right)$$

$$H_{10,13} = H_{11,14} = H_{24,27} = H_{25,28} = 2C_1 \cos\left(\frac{1}{2}\eta - \frac{1}{2}\zeta\right)$$

$$H_{10,14} = H_{11,13} = H_{24,28} = H_{25,27} = -2C_2 \cos\left(\frac{1}{2}\eta - \frac{1}{2}\zeta\right)$$

$$H_{10,27} = H_{11,28} = H_{24,13} = H_{25,14} = 2C_1 \cos\left(\frac{1}{2}\eta + \frac{1}{2}\zeta\right)$$

$$H_{10,28} = H_{11,27} = H_{24,14} = H_{25,13} = 2C_2 \cos\left(\frac{1}{2}\eta + \frac{1}{2}\zeta\right)$$

C. p - d interactions

$$H_{1,7} = H_{3,8} = H_{15,21} = H_{17,22} = -(pd\pi) \exp\left(i\frac{1}{2}\xi\right)$$

$$H_{1,9} = H_{2,11} = H_{15,23} = H_{16,25} = -(pd\pi) \exp\left(i\frac{1}{2}\eta\right)$$

$$H_{1,21} = H_{3,22} = H_{15,7} = H_{17,8} = (pd\pi) \exp\left(-i\frac{1}{2}\xi\right)$$

$$H_{1,23} = H_{2,25} = H_{15,9} = H_{16,11} = (pd\pi) \exp\left(-i\frac{1}{2}\eta\right)$$

$$H_{2,13} = H_{3,12} = H_{16,27} = H_{17,26} = -(pd\pi) \exp\left(i\frac{1}{2}\zeta\right)$$

$$\begin{aligned}
H_{2,27} = H_{3,26} = H_{16,13} = H_{17,12} &= (pd\pi) \exp\left(-i\frac{1}{2}\zeta\right) \\
H_{4,6} = H_{18,20} &= \frac{1}{2}(pd\sigma) \exp\left(i\frac{1}{2}\xi\right) \\
H_{4,10} = H_{18,24} &= \frac{1}{2}(pd\sigma) \exp\left(i\frac{1}{2}\eta\right) \\
H_{4,14} = H_{18,28} &= -(pd\sigma) \exp\left(i\frac{1}{2}\zeta\right) \\
H_{4,20} = H_{18,6} &= -\frac{1}{2}(pd\sigma) \exp\left(-i\frac{1}{2}\xi\right) \\
H_{4,24} = H_{18,10} &= -\frac{1}{2}(pd\sigma) \exp\left(-i\frac{1}{2}\eta\right) \\
H_{4,28} = H_{18,14} &= (pd\sigma) \exp\left(-i\frac{1}{2}\zeta\right) \\
H_{5,6} = H_{19,20} &= -\frac{\sqrt{3}}{2}(pd\sigma) \exp\left(i\frac{1}{2}\xi\right) \\
H_{5,10} = H_{19,24} &= \frac{\sqrt{3}}{2}(pd\sigma) \exp\left(i\frac{1}{2}\eta\right) \\
H_{5,20} = H_{19,6} &= \frac{\sqrt{3}}{2}(pd\sigma) \exp\left(-i\frac{1}{2}\xi\right) \\
H_{5,24} = H_{19,10} &= -\frac{\sqrt{3}}{2}(pd\sigma) \exp\left(-i\frac{1}{2}\eta\right)
\end{aligned}$$

TABLE III: TB basis functions used in the band-structure calculation of LSMO

	No.	Origin	Function	No.	Origin	Function
Fe 3d	1	(0, 0, 0)	xy	O 2p	6	$\frac{1}{2}a(1, 0, 0)$ x
	2	(0, 0, 0)	yz		7	$\frac{1}{2}a(1, 0, 0)$ y
	3	(0, 0, 0)	zx		8	$\frac{1}{2}a(1, 0, 0)$ z
	4	(0, 0, 0)	$3z^2 - r^2$		9	$\frac{1}{2}a(0, 1, 0)$ x
	5	(0, 0, 0)	$x^2 - y^2$		10	$\frac{1}{2}a(0, 1, 0)$ y
					11	$\frac{1}{2}a(0, 1, 0)$ z
					12	$\frac{1}{2}a(0, 0, 1)$ x
					13	$\frac{1}{2}a(0, 0, 1)$ y
					14	$\frac{1}{2}a(0, 0, 1)$ z

TABLE IV: Nonzero matrix elements of the TB Hamiltonian used in the calculation of LSMO. $\xi \equiv k_x a$, $\eta \equiv k_y a$, and $\zeta \equiv k_z a$.

A. d - d interactions

$$H_{1,1} = H_{2,2} = H_{3,3} = \epsilon_d - 4Dq - \Delta E/2 \text{ (up spin)}, \epsilon_d - 4Dq + \Delta E/2 \text{ (down spin)}$$

$$H_{4,4} = H_{5,5} = \epsilon_d + 6Dq - \Delta E/2 \text{ (up spin)}, \epsilon_d + 6Dq + \Delta E/2 \text{ (down spin)}$$

B. p - p interactions

$$C_1 = \frac{1}{2}(pp\sigma) + \frac{1}{2}(pp\pi), C_2 = \frac{1}{2}(pp\sigma) - \frac{1}{2}(pp\pi), C_3 = (pp\pi)$$

$$H_{6,6} = H_{10,10} = H_{14,14} = \epsilon_p$$

$$H_{7,7} = H_{8,8} = H_{9,9} = H_{11,11} = H_{12,12} = H_{13,13} = \epsilon_p$$

$$H_{6,9} = H_{7,10} = 4C_1 \cos(\frac{1}{2}\xi) \cos(\frac{1}{2}\eta)$$

$$H_{6,10} = H_{7,9} = -4C_2 \sin(\frac{1}{2}\xi) \sin(\frac{1}{2}\eta)$$

$$H_{6,12} = H_{8,14} = 4C_1 \cos(\frac{1}{2}\xi) \cos(\frac{1}{2}\zeta)$$

$$H_{6,14} = H_{8,12} = -4C_2 \sin(\frac{1}{2}\xi) \sin(\frac{1}{2}\zeta)$$

$$H_{7,13} = 4C_3 \cos(\frac{1}{2}\xi) \cos(\frac{1}{2}\zeta), H_{8,11} = 4C_3 \cos(\frac{1}{2}\xi) \cos(\frac{1}{2}\eta)$$

$$H_{9,12} = 4C_3 \cos(\frac{1}{2}\eta) \cos(\frac{1}{2}\zeta)$$

$$H_{10,13} = H_{11,14} = 4C_1 \cos(\frac{1}{2}\eta) \cos(\frac{1}{2}\zeta)$$

$$H_{10,14} = H_{11,13} - 4C_2 \sin(\frac{1}{2}\eta) \sin(\frac{1}{2}\zeta)$$

C. p - d interactions

$$H_{1,7} = H_{3,8} = -2i(pd\pi) \sin(\frac{1}{2}\xi)$$

$$H_{1,9} = H_{2,11} = -2i(pd\pi) \sin(\frac{1}{2}\eta)$$

$$H_{2,13} = H_{3,12} = -2i(pd\pi) \sin(\frac{1}{2}\zeta)$$

$$H_{4,6} = i(pd\sigma) \sin(\frac{1}{2}\xi), H_{4,10} = i(pd\sigma) \sin(\frac{1}{2}\eta)$$

$$H_{4,14} = -2i(pd\sigma) \sin(\frac{1}{2}\zeta), H_{5,6} = -\sqrt{3}i(pd\sigma) \sin(\frac{1}{2}\xi)$$

$$H_{5,10} = \sqrt{3}i(pd\sigma) \sin(\frac{1}{2}\eta)$$

* Electronic address: wadati@wyvern.phys.s.u-tokyo.ac.jp

- [1] M. Imada, A. Fujimori, and Y. Tokura, *Rev. Mod. Phys.* **70**, 1039 (1998).
- [2] J. Zaanen, G. A. Sawatzky, and J. W. Allen, *Phys. Rev. Lett.* **55**, 418 (1985).
- [3] T. Yoshida, K. Tanaka, H. Yagi, A. Ino, H. Eisaki, A. Fujimori, and Z.-X. Shen, *Phys. Rev. Lett.* **95**, 146404 (2005).
- [4] M. Izumi, Y. Konishi, T. Nishihara, S. Hayashi, M. Shinohara, M. Kawasaki, and Y. Tokura, *Appl. Phys. Lett.* **73**, 2497 (1998).
- [5] J. Choi, C. B. Eom, G. Rijnders, H. Rogalla, and D. H. A. Blank, *Appl. Phys. Lett.* **79**, 1447 (2001).
- [6] K. Horiba, H. Oguchi, H. Kumigashira, M. Oshima, K. Ono, N. Nakagawa, M. Lippmaa, M. Kawasaki, and H. Koinuma, *Rev. Sci. Instr.* **74**, 3406 (2003).
- [7] M. Shi, M. C. Falub, P. R. Willmott, J. Krempasky, R. Herger, K. Hricovini, and L. Patthey, *Phys. Rev. B* **70**, 140407 (2004).
- [8] A. Chikamatsu, H. Wadati, H. Kumigashira, M. Oshima, A. Fujimori, N. Hamada, T. Ohnishi, M. Lippmaa, K. Ono, M. Kawasaki, and H. Koinuma, cond-mat/0503373, *Phys. Rev. B*, in press.
- [9] H. Wadati, A. Chikamatsu, M. Takizawa, R. Hashimoto, H. Kumigashira, T. Yoshida, T. Mizokawa, A. Fujimori, M. Oshima, M. Lippmaa, M. Kawasaki, and H. Koinuma, cond-mat/0603333.
- [10] V. N. Strocov, *J. Electron Spectrosc. Relat. Phenom.* **130**, 65 (2003).
- [11] A. Liebsch, *Phys. Rev. Lett.* **90**, 096401 (2003).
- [12] A. H. Kahn and A. J. Leyendecker, *Phys. Rev.* **135**, A1321 (1964).
- [13] L. F. Mattheiss, *Phys. Rev.* **181**, 987 (1969).
- [14] L. F. Mattheiss, *Phys. Rev. B* **6**, 4718 (1972).
- [15] J. C. Slater and G. F. Koster, *Phys. Rev.* **94**, 1498 (1954).
- [16] W. A. Harrison, *Electronic Structure and the Properties of Solids* (Dover, New York, 1989).
- [17] L. F. Mattheiss, *Phys. Rev. B* **5**, 290 (1972).
- [18] A. E. Bocquet, T. Mizokawa, T. Saitoh, H. Namatame, and A. Fujimori, *Phys. Rev. B* **46**, 3771 (1992).

- [19] H. Wadati, D. Kobayashi, H. Kumigashira, K. Okazaki, T. Mizokawa, A. Fujimori, K. Horiba, M. Oshima, N. Hamada, M. Lippmaa, M. Kawasaki, and H. Koinuma, *Phys. Rev. B* **71**, 035108 (2005).
- [20] I. H. Inoue, I. Hase, Y. Aiura, A. Fujimori, Y. Haruyama, T. Maruyama, and Y. Nishihara, *Phys. Rev. Lett.* **74**, 2539 (1995).
- [21] I. H. Inoue, O. Goto, H. Makino, N. E. Hussey, and M. Ishikawa, *Phys. Rev. B* **58**, 4372 (1998).
- [22] A. Sekiyama, H. Fujiwara, S. Imada, S. Suga, H. Eisaki, S. I. Uchida, K. Takegahara, H. Harima, Y. Saitoh, I. A. Nekrasov, G. Keller, D. E. Kondakov, A. V. Kozhevnikov, T. Pruschke, K. Held, D. Vollhardt, and V. I. Anisimov, *Phys. Rev. Lett.* **93**, 156402 (2004).
- [23] K. Takegahara, *J. Electron Spectrosc. Relat. Phenom.* **66**, 303 (1994).
- [24] I. H. Inoue, C. Bergemann, I. Hase, and S. R. Julian, *Phys. Rev. Lett.* **88**, 236403 (2002).
- [25] K. Maiti, P. Mahadevan, and D. D. Sarma, *Phys. Rev. Lett.* **80**, 2885 (1998).
- [26] D. Kalkstein and P. Soven, *Surf. Sci.* **26**, 85 (1971).
- [27] M. Takano, J. Kawachi, N. Nakanishi, and Y. Takeda, *J. Solid. State Chem.* **39**, 75 (1981).
- [28] J. Matsuno, T. Mizokawa, A. Fujimori, K. Mamiya, Y. Takeda, S. Kawasaki, and M. Takano, *Phys. Rev. B* **60**, 4605 (1999).
- [29] T. Arima, Y. Tokura, and J. B. Torrance, *Phys. Rev. B* **48**, 17006 (1993).
- [30] A. Urushibara, Y. Moritomo, T. Arima, A. Asamitsu, G. Kido, and Y. Tokura, *Phys. Rev. B* **51**, 14103 (1995).
- [31] J.-H. Park, E. Vescovo, H.-J. Kim, C. Kwon, R. Ramesh, and T. Venkatesan, *Nature* **392**, 794 (1998).
- [32] K. Horiba, A. Chikamatsu, H. Kumigashira, M. Oshima, N. Nakagawa, M. Lippmaa, K. Ono, M. Kawasaki, and H. Koinuma, *Phys. Rev. B* **71**, 155420 (2005).
- [33] T. Okuda, A. Asamitsu, Y. Tomioka, T. Kimura, Y. Taguchi, and Y. Tokura, *Phys. Rev. Lett.* **81**, 3203 (1998).
- [34] A. Fujimori, A. Ino, J. Matsuno, T. Yoshida, K. Tanaka, and T. Mizokawa, *J. Electron Spectrosc. Relat. Phenom.* **124**, 127 (2002).